Journal of Materials Chemistry A

Accepted Manuscript

ROYAL SOCIETY OF CHEMISTRY

www.rsc.org/materialsA

Hierarchical core-shell heterostructure of porous carbon nanofiber@$ZnCo_2O_4$ nanoneedle arrays: Advanced binder-free electrodes for all-solid-state supercapacitors

Hao Niu, Xue Yang, He Jiang, Dan Zhou, Xin Li, Ting Zhang, Jiuyu Liu, Qian Wang*, Fengyu Qu*

College of Chemistry and Chemical Engineering, Harbin Normal University, Harbin 150025, China

Abstract

Hierarchical $ZnCo_2O_4$ nanoneedle arrays are vertically grown on porous carbon nanofibers (PCFs) to form core-shell heterostructure through a facile hydrothermal method followed by thermal treatment. Such unique configuration makes full use of the synergistic effects from both excellent electrical conductivity of PCFs and high specific capacitance of $ZnCo_2O_4$, endowing the hybrid to be an excellent electrode for flexible supercapacitors. Benefiting from their intriguing structural features, the PCF@$ZnCo_2O_4$ hybrid possesses fascinating electrochemical performance as integrated binder-free electrode for supercapacitors. Remarkably, this PCF@$ZnCo_2O_4$ electrode could achieve a high capacitance of 1384 F g^{-1} at a scan rate of 2 mV s^{-1}. Besides, an all-solid-state asymmetric supercapacitor fabricated with the as-prepared PCF@$ZnCo_2O_4$ hybrid as positive electrode and PCFs as negative electrode achieves a high energy density of 49.5 Wh kg^{-1} (based on the total mass of the material on the two electrodes) at a power density of 222.7 W kg^{-1}. Furthermore, the all-solid-state asymmetric supercapacitor device exhibits remarkable cycling stability with 90% specific capacitance retention after 3000 cycles. Therefore, these fascinating electrochemical performances make this material hold great promise for next generation high-energy supercapacitor applications.

*Corresponding authors. Tel. /fax: +86 451 88060653.
E-mail addresses: wangqianhrb@163.com (Q. Wang); qufengyuhsd@163.com (F.Y. Qu).

1. Introduction

Nowadays, there has been an ever increasing and urgent demand to seek for clean and renewable energy sources because of the increased concerns over environmental pollution caused by the conventional energy technologies and rapid depletion of non-renewable resources.[1-7] Thus exploiting high-performance energy-related materials for energy storage devices is highly urgent and still remains a major challenge.[8-10] As one of the most promising types of energy storage devices, supercapacitors have attracted tremendous interest as power sources for applications requiring fast bursts of energy or as back-up power sources in electric vehicles owning to their desirable properties like high power density,[11,12] fast charge/discharge rate[13] and superior cycling stability.[14-18] Generally, supercapacitors can be classified into two types based on the underlying energy storage mechanism: electrical double-layer capacitors and pseudocapacitors.[19,20] Pseudocapacitors could make full use of reversible Faradic reactions that occurred at the surface of electrode, offering competitive capacitance compared with electrical double-layer capacitors, which store electrical energy in the electric double-layer near the interfaces between electrode and electrolyte.[21]

Pseudocapacitive materials, mainly including transition metal oxides/hydroxides (MnO_2,[22,23] Co_3O_4[24] and NiO[25]) and electrically conducting polymers (polyaniline[26] and polypyrrole[27,28]) have been extensively investigated as promising electrode materials for supercapacitors during the past decades. However, these materials often suffer from low electrical conductivity and serious structural degradation during cycling process, which significantly deteriorates its power capability at high rates and leads to poor cycling performance, greatly limiting its practical application.[29] Therefore, it is necessary to exploit advanced/novel electrode materials to enhance the energy density, power capability and cycling stability to meet the further application. Considerable recent research have been focused on ternary metal oxides, which could achieve higher specific capacitance than the corresponding single-component metal oxides since they can offer richer redox chemistry and combine the contributions from both metal ions.[30] A series of ternary oxides have been developed as

pseudocapacitive electrode materials for supercapacitors, such as $NiCo_2O_4$,[31] $MnCo_2O_4$ and $CoMn_2O_4$[32] and $ZnCo_2O_4$.[33,34] $ZnCo_2O_4$, replacing one cobalt atom by zinc, has been considered as an alternative candidate as electrode material for supercapacitors.[33,34] With a cubic spinel structure, Zn ions occupy the tetrahedral sites and the trivalent Co ions occupy the octahedral sites, revealing brilliant electroactivity than single cobalt oxides.[3] In addition, Zn elements have other advantages, including low cost, abundant resources and environmental friendliness and so on. Considering these points, various nanostructured $ZnCo_2O_4$, such as nanorods,[35] nanowires,[36,37] nanotubes,[37] porous microspheres,[38] nanosheets,[39] and core-shell structures[33,40] have been intensively investigated as electrode materials for supercapacitors in recent years.

Design and synthesis of advanced electrodes for supercapacitors with excellent electrical conductivity, short ion transport/diffusion path, direct and intimate contact between active materials and electrolytes without the assistance of a binder are of significant importance to further commercial application. The core/shell nanofiber arrays with a conductive core are expect to exhibit a robust structure through taking full advantage of the synergistic effects between a highly conductive one-dimensional nanostructure core and electroactive transition metal oxide shell. Therefore, considerable effort has been devoted to synthesizing core/shell nanostructure for high-performance supercapacitors.[41,42]

In this work, we developed the synthesis of unique hierarchical $ZnCo_2O_4$ nanoneedle arrays vertically grown on porous carbon nanofibers (PCFs) to form core-shell heterostructure through a facile hydrothermal approach followed by heating treatment as binder-free electrodes for electrochemical energy-storage application. The $ZnCo_2O_4$ nanoneedle arrays are composed of numerous highly crystalline nanoparticles, leaving a large number of mesopores for fast ion transport and effectively alleviating the volume change during the charge/discharge process. The PCF@$ZnCo_2O_4$ hybrid can be straightforwardly used as binder-free electrodes for supercapacitors, exhibiting a high specific capacitance of 1384 F g^{-1} at a scan rate of 2 mV s^{-1} in 6 M KOH aqueous

solution. Meanwhile, a high performance all-solid-state asymmetric supercapacitor (ASC) device with PCF@$ZnCo_2O_4$ as the positive electrode and PCFs as the negative electrode achieves a remarkable energy density of 49.5 Wh kg^{-1} at a power density of 222.7 W kg^{-1} based on the total mass of material on two electrodes. Moreover, the fabricated ASC device could retain 90% of its initial capacitance after 3000 cycles. This work may pave a promising way to rationally design and fabricate novel $ZnCo_2O_4$-based nanostructured electrode free of additives for high-performance energy storage/conversion devices.

2 Experimental section

2.1. Preparation of phenol-formaldehyde resins

For the preparation of resin precursor, 0.61 g of phenol was melted at 42 ℃ and mixed with 0.15 mL of NaOH aqueous solution (20 wt.%) under stirring. Then, 1.05 g of formalin (37 wt.%) was added into the above mixture below 50 ℃. Afterwards, the mixture was stirred at 70 ℃ for 1 h, followed by cooling down to room temperature naturally. Subsequently, the pH value of the system was adjusted to neutral through addition of 0.6 M HCl solution. Finally, the residual water was removed by using rotary evaporation below 50 ℃.

2.2. Preparation of PCFs

PCFs were prepared through a facile electrospinning method. Typically, 0.5 g of triblock copolymer Pluronic (P123) and 1.4 g of polyvinyl pyrrolidone (PVP) were dissolved in 10 mL of ethanol under vigorous stirring for 1 h. Next, 0.1 mL (2 M) of HCl, 3 mL of tetraethyl orthosilicate (TEOS), and 0.4 g of resin precursors were added to form a mixture and stirred for 4 h. Subsequently, the viscous solution was loaded into a 5-mL plastic syringe equipped with a 9-gauge stainless steel nozzle. The solution was electrospun at a voltage of 18 kV. The as-electrospun nanofibers were collected on an aluminum foil and the distance between the nozzle tip and the collector was

maintained at 15 cm. The as-collected films were dried at room temperature for 24 h followed by heat treatment in an oven at 100 °C for 24 h. After that, the fibers were carbonized at 800 °C for 4 h under N_2 with a heating rate of 2 °C min^{-1}. Finally, the silica template was removed with 10 wt.% hydrofluoric acid solution and the obtained PCF fabrics were filtrated and washed repeatedly with distilled water for several times and dried at 60 °C for 12 h.

2.3. Preparation of herarchical PCF@$ZnCo_2O_4$ hybrid

The growth of $ZnCo_2O_4$ nanoneedle arrays on PCFs were achieved through a typical hydrothermal synthesis method combined with a calcination procedure. Typically, 0.01 mol of zinc nitrate hexahydrate ($Zn(NO_3)_2 \cdot 6H_2O$), 0.02 mol of cobalt nitrate hexahydrate ($Co(NO_3)_2 \cdot 6H_2O$), 0.05 mol of urea ($CO(NH_2)_2$) and 0.02 mol of ammonium fluoride (NH_4F) were dissolved in 30 mL deionized water under constant magnetic stirring to form a clear red solution. Then the PCF substrate was immersed into the above solution and left to stand for 2 h. Afterwards, the above solution and the PCF substrate were transferred into a 40 mL Teflon-lined stainless steel autoclave, which was sealed and maintained at 120 °C for 5 h in an electric oven. After the autoclave was cooled down to room temperature naturally, the sample was collected, rinsed several times with distilled water and dried in a vacuum oven at 80 °C over night, followed by annealed at 400 °C in N_2 atmosphere for 2 h with a heating rate of 2 °C min^{-1} to obtain PCF@$ZnCo_2O_4$ hybrid. For comparison, pure $ZnCo_2O_4$ sample was also prepared through the same synthesis procedure without the presence of PCF substrate.

2.4. Material characterizations

The crystallographic structures of the materials were determined by X-ray diffraction (XRD) equipped with Cu Kα radiation (λ = 0.15406 nm). X-ray photoelectron spectroscopy (XPS) was characterized using a PHI 5000 ESCA X-ray photoelectron spectrometer with a monochromated Al

Kα X-ray source (1486.6 eV) to investigate the chemical structure of the materials. The thermal behavior of the materials was analyzed by thermogravimetric analysis (TGA) and differential thermal analysis (DTA, TG-209) in air atmosphere. The nitrogen adsorption/desorption, surface areas, and average pore sizes were measured using a Quantachrome NOVA 2000e analyzer. Specific surface areas and pore size distributions were calculated using the Brunauer-Emmett-Teller (BET) and density-functional-theory (DFT) or Barrett-Joyner-Halenda (BJH) models from the adsorption branches, respectively. The microstructure of the samples was investigated by field-emission scanning electron microscopy (SEM, Hitachi S-4800) and transmission electron microscopy (TEM, Tecnai F20).

2.5. Electrochemical measurements

All the electrochemical measurements were performed on a CHI 660D electrochemical workstation at room temperature. The working electrodes were fabricated through pressing active material (3.8 mg) between two pieces of Ni foam under 6 MPa. The electrochemical studies of the individual electrode were carried out with a three-electrode system in 6 M KOH aqueous electrolyte, in which the fabricated electrodes, platinum foil and saturated calomel electrode (Hg/HgO) were used as the working, counter and reference electrodes, respectively.

Cyclic voltammetry (CV) tests were done between 0 to 0.45 V (vs. Hg/HgO) at different scan rates. The galvanostatic charge-discharge curves were measured from 3 to 20 A g^{-1} within the potential window of 0 to 0.45 V (vs. Hg/HgO) and the electrochemical impedance spectroscopy (EIS) measurements were carried out in the frequency range from 100 kHz to 0.01 Hz at open circuit potential with an AC amplitude of 5 mV. The specific capacitance of the electrode can be calculated based on the CV curves according to the following equation:

$$C = \int IdV / vmV \quad (1)$$

where I is the response current density, V is the potential, v is the scan rate, and m is the total mass of the material on the electrodes.

2.6. Fabrication of all-solid-state ASC device

The electrochemical performance of the hybrid was further characterized using an all-solid-state ASC device with the prepared PCF@$ZnCo_2O_4$ hybrid and PCFs as the positive and negative electrodes, respectively. The polyvinylacetate (PVA)/KOH polymer gel electrolyte was prepared as follows: 4.2 g of PVA and 4.2 g of KOH were mixed in 50 mL of distilled water. The mixture was heated up to 85 °C under vigorous stirring until the solution became clear. Subsequently, the electrodes and the cellulose acetate membrane separator were immersed in the PVA/KOH gel for 1 h. After fabrication, the assembled ASC device was dried in a fume hood at room temperature overnight to evaporate the excess water.

The mass ratio of the negative electrode to the positive electrode was decided based on charge balance theory ($q_+ = q_-$). The charge stored (q) by each electrode depends on the following equation:

$$q = C \times \Delta V \times m \tag{2}$$

The power density (P) and energy density (E) of the supercapacitor devices were calculated based on the following equations:

$$E = \frac{1}{2} C \Delta V^2 \tag{3}$$

$$P = \frac{E}{t} \tag{4}$$

where C is the specific capacitance of the ASC device calculated according to the CV curves based on the total weight of the materials in two electrodes, ΔV is the voltage scan range and t is the discharge time.

3. Results and discussion

3.1. Structure and morphology of the PCF@$ZnCo_2O_4$ hybrid

The synthetic procedure of PCF@$ZnCo_2O_4$ hybrid is illustrated in Scheme 1. Firstly, the PCF substrate is obtained through a facile electrospinning method followed by thermal treatment in N_2 atmosphere at high temperature. Subsequently, the Zn-Co precursor was successfully grown on the surface of PCF substrate through a hydrothermal reaction. Finally, the as-synthesized PCF@Zn-Co precursor was annealed at 400 °C to allow the Zn-Co precursor to transform into $ZnCo_2O_4$ nanoneedle array to form the hierarchical PCF@$ZnCo_2O_4$ heterostructure.

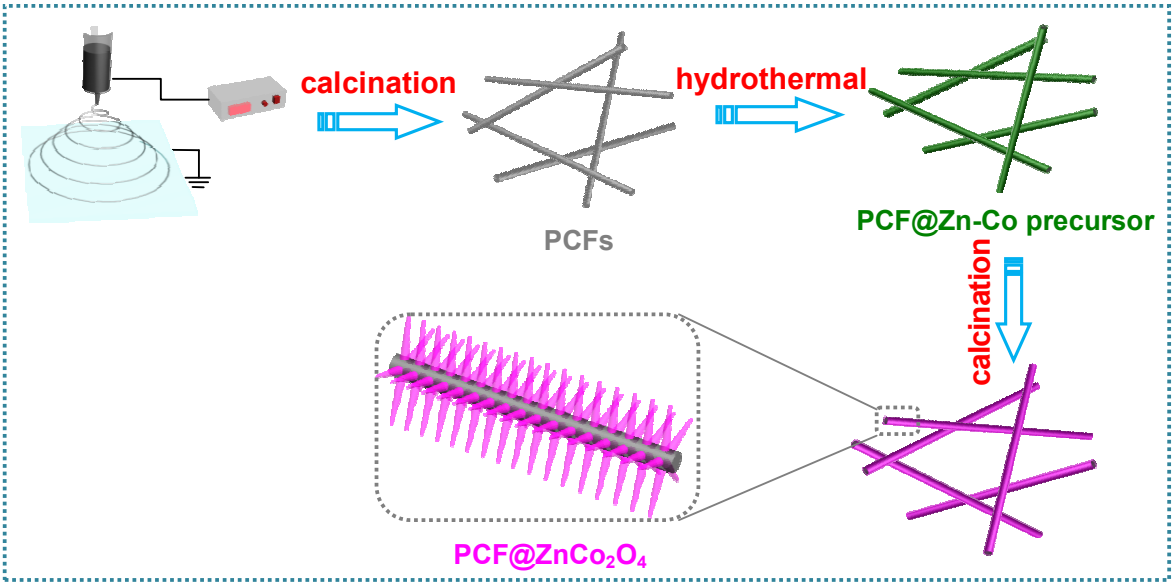

Scheme 1. Schematic illustration of the fabrication of PCF@$ZnCo_2O_4$ hybrid.

Fig. 1a displays typical SEM image of as-prepared PCFs. Obviously, highly uniform carbon nanofibers can be easily obtained through a facile electrospinning method. As is shown, the electrospun nanofibers exhibit relatively smooth surface with an average diameter of around 350 nm. Additionally, these nanofibers interweave with each other to form a three-dimensional conductive network configuration. From the high magnification TEM image (Fig. 1b), we can see that the PCFs are composed of the graphitic planner structure and considerable micropores and mesopores exist in the carbon fibers, which could be attributed to the decomposition of the polymer and removal of

SiO_2 template.[43,44] Fig. 1c shows the nitrogen adsorption-desorption isotherms of the as-prepared PCFs, which exhibits a combined typical I/IV isotherms with an obvious H3 hysteresis loop at relatively low pressure, confirming the existence of micropores in the sample as a result of the decomposition of the polymer.[45,46] The BET specific surface area of the PCFs is calculated to be as high as 1939 m^2 g^{-1}. The pore size distribution of PCFs obtained from the adsorption branch of the isotherm is showed in Fig. 1d, indicating that the pore size is mainly in the microporous range (about 1.1 nm and 1.5 nm) and mesoporous range (about 3 nm), which is in good agreement with the TEM image.

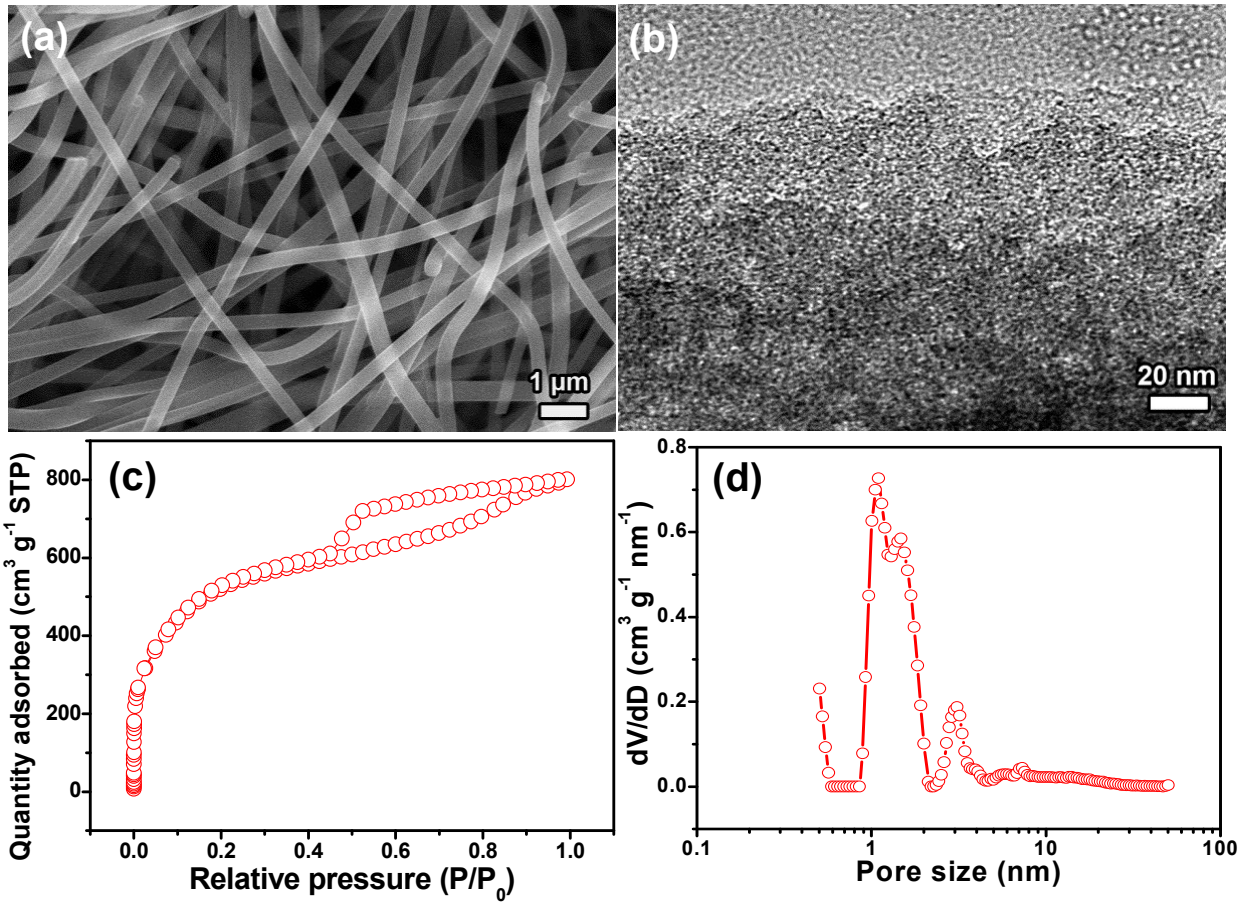

Fig. 1. (a) SEM and (b) high magnification TEM images of the PCFs. (c) Nitrogen adsorption-desorption isotherm and (d) pore size distribution of the PCFs.

The structure and morphology of the as-synthesized hierarchical PCF@$ZnCo_2O_4$ hybrid were characterized by SEM. After the hydrothermal reaction and thermal treatment, the smooth surface of PCFs becomes relatively fluffy compared with that of the pristine PCFs. Numerous densely-packed acicular $ZnCo_2O_4$ nanoneedle arrays grow uniformly on the skeletons of PCF substrate to form large-scale conformal core-shell naostrucures as shown in Fig. 2a. The $ZnCo_2O_4$ nanoneedle arrays seem like considerable grass growing perpendicularly to the surface of PCF substrate. High-magnification SEM image shown in Fig. 2b clearly depicts that the PCF@$ZnCo_2O_4$ hybrid has uniform diameter of ~3 μm and the $ZnCo_2O_4$ nanoneedle arrays have uniform diameters of 30 nm at the middle section and lengths of about 1.3 μm. It is worth noting that each $ZnCo_2O_4$ nanoneedle with a rough surface is composed of numerous nanoparticles accumulating with each other to form a highly porous structure due to the release of gaseous species during the calcination process (Fig. 2c). In addition, the meso/macropores among adjacent nanoneedles would facilitate the rapid penetration of the electrolyte ions into the porous structures, which will significantly decrease the transport/migration path of electrolyte ions during the charge/discharge process. In contrast, without the presence of PCF substrate, $ZnCo_2O_4$ nanoneedles tend to self-assemble into micro-flowers with diameter of approximately 4 μm under same synthesis condition (Fig. 2d). The crystallographic structure of the materials were analyzed by XRD as shown in Fig. 2e. All the diffraction peaks of the XRD pattern for $ZnCo_2O_4$ can be readily indexed to cubic spinel $ZnCo_2O_4$ phase (JCPDS card no 23-1390; space group: *Fd3m*).[47] With regard to pristine PCF substrate, the diffraction peaks located at 23.2° and 43.1° can be assigned to the (002) and (100) reflection planes of graphite, respectively.[48] Except for the reflections owing to PCFs, all the other diffraction peaks in the XRD pattern of PCF@$ZnCo_2O_4$ hybrid could be well-ascribed to spinel $ZnCo_2O_4$ phase, definitely confirming the successful growth of $ZnCo_2O_4$ nanoneedle arrays on the surface of PCFs.

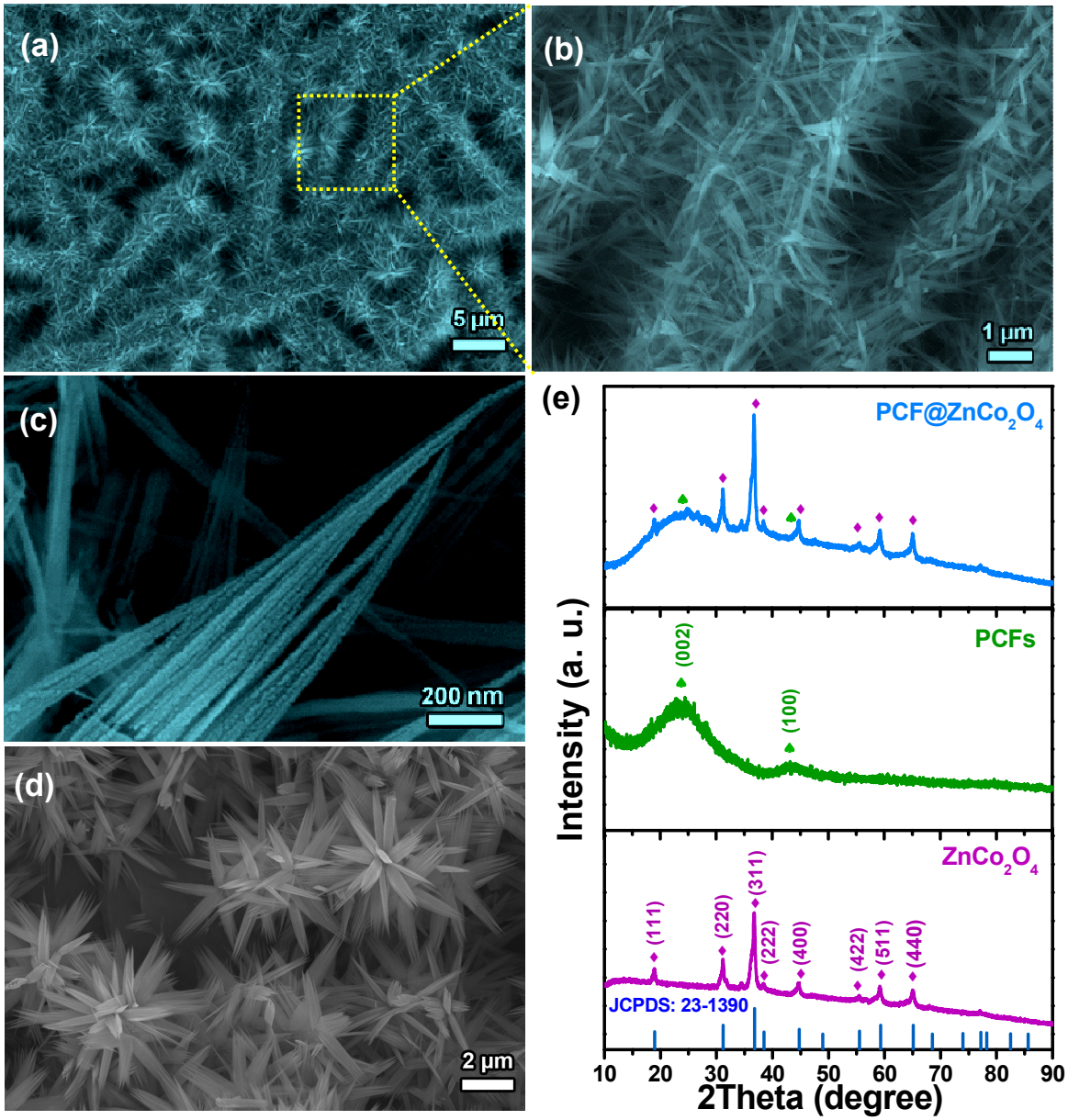

Fig. 2. (a-c) Typical SEM images of PCF@$ZnCo_2O_4$ hybrid. (d) SEM image of pure $ZnCo_2O_4$ micro-flowers. (e) XRD patterns of $ZnCo_2O_4$, PCFs and PCF@$ZnCo_2O_4$ hybrid.

TEM measurement and selected area electron diffraction (SAED) are carried out to further investigate the detailed microstructure of the as-synthesized PCF@$ZnCo_2O_4$ hybrid. As shown in Fig. 3a and b, the $ZnCo_2O_4$ nanoneedles are porous and the diameter of the nanoneedles gradually decreases from the root to the tip (~ 30 nm in diameter at the middle section), which matches well with the above SEM observation. In addition, the $ZnCo_2O_4$ nanoneedles are actually composed of

numerous small nanocrystals with the size of about 10 nm instead of the conventional single-crystalline nanoneedle and these nanocrystals interconnect with each other forming a stable porous structure, which is advantageous for the electrolyte diffusion and enhances the electrochemical activity.

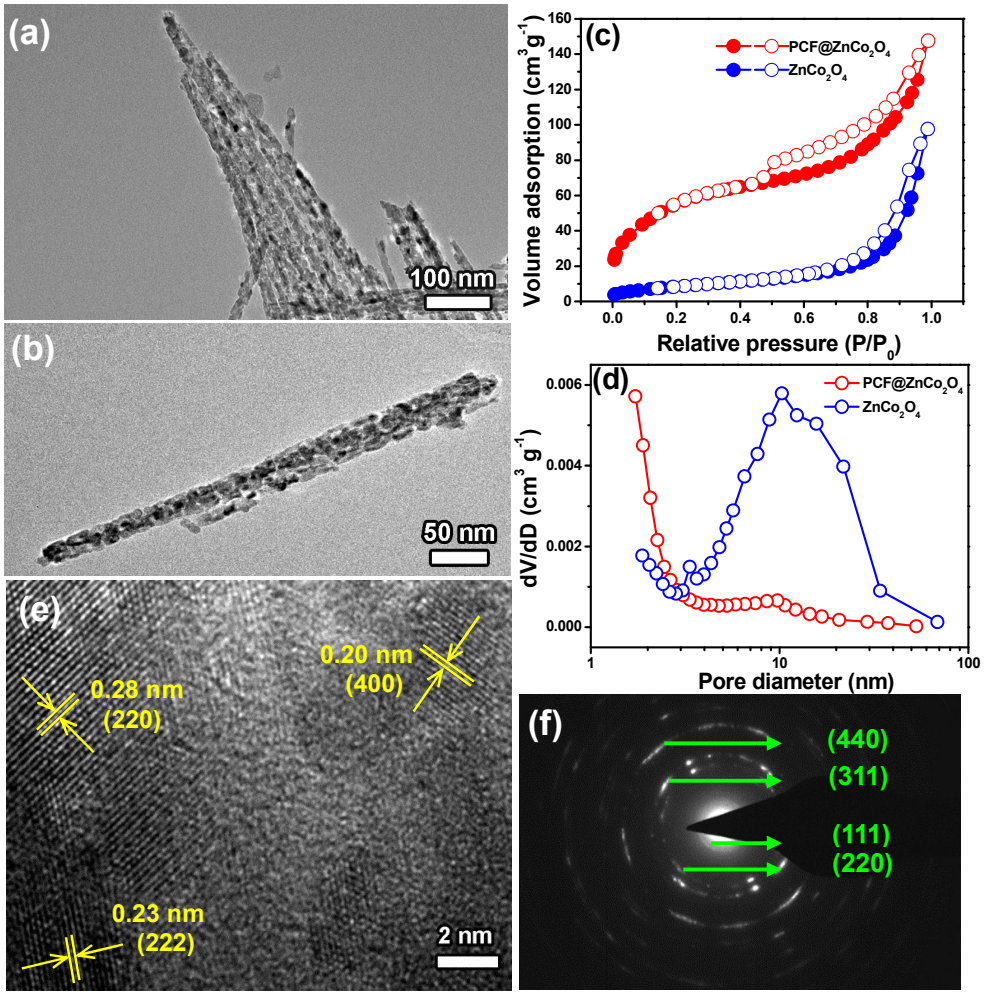

Fig. 3. (a and b) TEM characterization of $ZnCo_2O_4$ nanoneedles. (c) Nitrogen adsorption–desorption isotherm and (d) pore size distribution of the $ZnCo_2O_4$ and PCF@$ZnCo_2O_4$ hybrid. (e) High-resolution TEM image of the as-obtained $ZnCo_2O_4$ nanoneedles. (f) Corresponding SAED pattern from an individual nanoneedle.

Nitrogen isothermal adsorption-desorption measurments were performed to determine the porosity and surface area of the materials. Both of the nitrogen adsorption-desorption isotherms of the two samples exhibit a typical IV isotherm with H3-type hysteresis loop, demonstrating the

presence of narrow slit-shaped mesopores (Fig. 3c). The BET specific surface area of the PCF@$ZnCo_2O_4$ is calculated to be 196 $m^2 g^{-1}$, which is much higher than that of pure $ZnCo_2O_4$ (31.7 $m^2 g^{-1}$). The pore size distribution of the $ZnCo_2O_4$ calculated from the adsorption data using the BJH modal shows a wide peak centered at 10.3 nm, which further confirms the mesoporous structure of $ZnCo_2O_4$ nanoneedles (Fig. 3d). By contrast, in addition to the mesopores centered at 9.7 nm, considerable micropores with size below 2 nm could be clearly found for the PCF@$ZnCo_2O_4$ hybrid, which is attributed to the micropores in PCFs substrate. By virtue of its large surface area and porous structure, the PCF@$ZnCo_2O_4$ nanoneedle is beneficial in electrical storage applications.

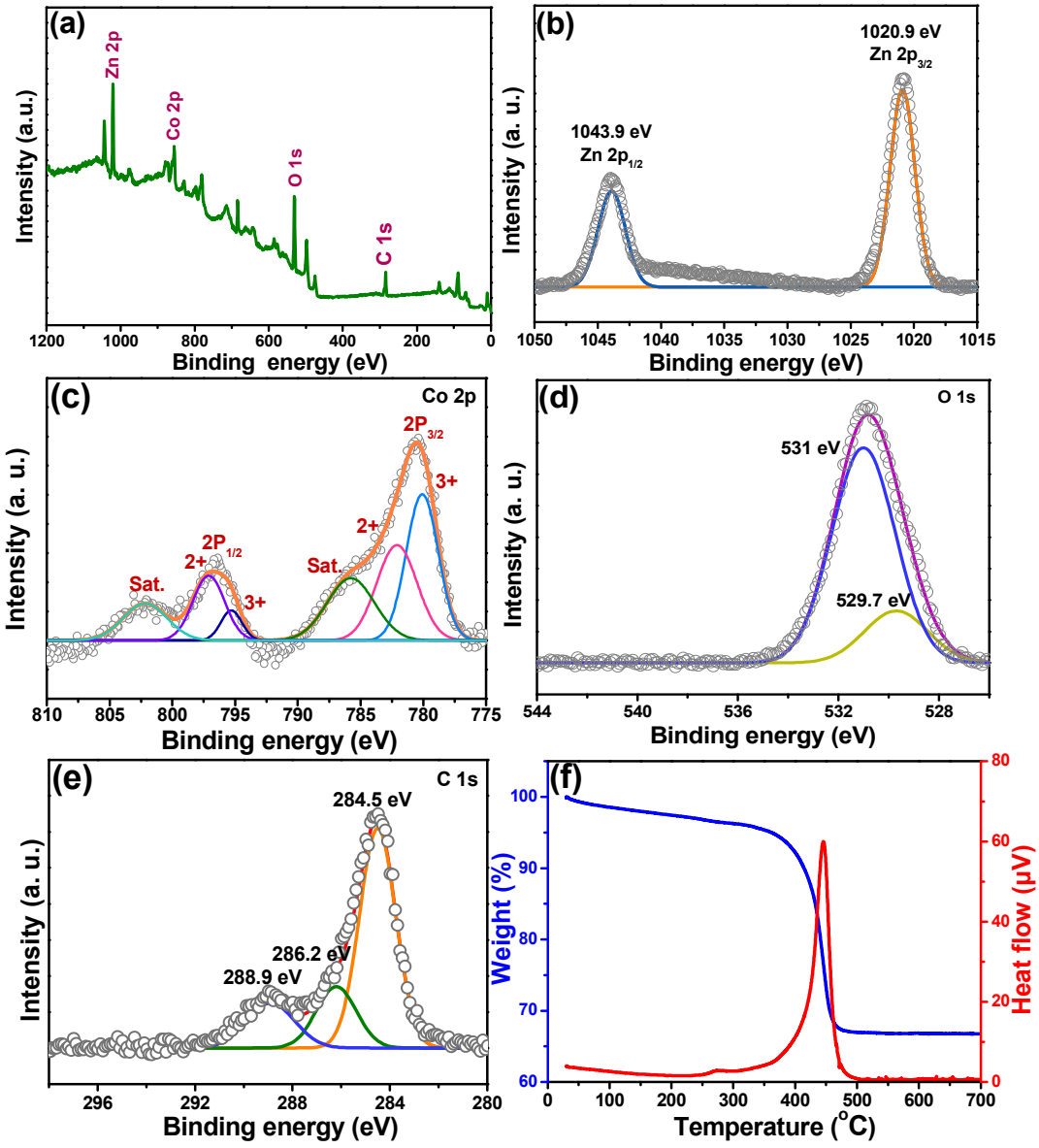

Fig. 4. (a) XPS survey spectrum of PCF@$ZnCo_2O_4$ hybrid. (b-e) XPS deconvoluted scans of (b) Zn 2p, (c) Co 2p, (d) O 1s and (e) C 1s. (f) TGA and DTA curves of the as-prepared PCF@$ZnCo_2O_4$ hybrid.

The surface electronic state of the elements and the composition of PCF@$ZnCo_2O_4$ hybrid were analyzed by XPS analysis and the corresponding results are given in Fig. 4. The full-survey-scan spectrum shown in Fig. 4a confirms the presence of Zn, Co and O elements along with a small quantity of C in the PCF@$ZnCo_2O_4$ hybrid. The Zn 2p deconvoluted spectrum exhibits two strong peaks at the binding energy of 1020.9 and 1043.9 eV (Fig. 4b), corresponding to Zn $2p_{3/2}$ and Zn $2p_{1/2}$ levels, respectively, and the spin-energy separation of 23 eV is the typical characteristic of Zn^{2+}.[49] The Co 2p spectrum can also be fitted with two spin-orbit doublets, characteristic of Co^{2+} and Co^{3+}, and two shake-up satellites (indicated as "Sat", Fig. 4c).[50,51] The binding energies at around 797.2 and 782.1 eV correspond to Co^{2+}, while the binding energies at around 795.4 and 780.1 eV attribute to Co^{3+}. The O 1s spectrum can also be deconvoluted into two components centered at 531 and 529.7 eV (Fig. 4d). The former peak corresponds to the absorption of oxygen and water molecules on the composite surface,[18] while the latter is attributed to the O^{2-} forming oxide with Co and Zn elements.[52] Fig. 4e demonstrates the deconvolution of C 1s spectrum with different oxygen containing functional groups which can be assigned to non-oxygenated C in C-C at 284.5 eV, the carbon in C-O at 286.4 eV, and the carbon in C=O at 288.8 eV.[53] Based on the obtained XPS data, the content of $ZnCo_2O_4$ in the hybrid is estimated to be 69.2 wt.%. TGA was carried out to further determine the weight percentage of $ZnCo_2O_4$ in the hybrid. TGA and DTA profiles for PCF@$ZnCo_2O_4$ hybrid are plotted in Fig. 4f. The sample undergoes a weight loss of 32.5 wt.% in a temperature range from room temperature to 700 °C with a heating rate of 5 °C min^{-1}. The weight loss (3.8 wt.%) below 300 °C is assigned to evaporation of moisture and the adsorbed water. The following significant weight loss (28.7 wt.%) between 300 °C and 700 °C is assigned to the

decomposition of PCFs. Thus the mass loading of $ZnCo_2O_4$ in the PCF@$ZnCo_2O_4$ hybrid could be estimated to be about 67.5 wt.% from the TGA curve.

3.2. Electrochemical characterization of PCF@$ZnCo_2O_4$ hybrid

The electrochemical properties of the PCF@$ZnCo_2O_4$ hybrid were firstly examined by CV and galvanostatic discharge-charge measurements with a three-electrode device in 6 M KOH aqueous electrolyte. Fig. 5a shows the CV curves of pure $ZnCo_2O_4$ and PCF@$ZnCo_2O_4$ electrode at a scan rate of 2 mV s^{-1}. Noticeably, the CV curve of the PCF@$ZnCo_2O_4$ hybrid electrode possesses much larger integrated area than that of $ZnCo_2O_4$ and PCF@Co_3O_4 (Fig. S1) implying that the PCF@$ZnCo_2O_4$ hybrid possesses a much higher specific capacitance at the same scan rate. Fig. 5b shows the typical CV curves of the PCF@$ZnCo_2O_4$ hybrid electrode within the potential range from 0 to 0.45 V (vs. Hg/HgO) at various scan rates. The shape of all the CV curves seriously deviates from ideal rectangular shape which is indicative of an electric double layer capacitor and all the CV curves exhibit a pair of well-defined redox peaks, indicating that the capacitance is mainly contributed by pseudocapacitance rather than electric double layer capacitance due to Faradic redox reactions. Specially, a pair of strong redox peak occurred around 0.14/0.24 V (vs. Hg/HgO) can be clearly observed at the scan rates from 2 to 50 mV s^{-1}, which mainly associated with the Faradic redox reactions related to Co-O/Co-O-OH as following equations.[30,54,55]

$$CoOOH + H_2O + e^- \leftrightarrow Co(OH)_2 + OH^- \quad (5)$$

$$Co_2O_4^{2-} + 2H_2O \leftrightarrow 2CoOOH + 2OH^- \quad (6)$$

Additionally, the current densities of redox peaks almost increases linearly with the increase of scan rates, demonstrating that the excellent kinetics of interfacial Faradic redox reactions and the rapid transport of electrons and ions. Also, upon the increase of the scan rate from 2 to 50 mV s^{-1}, the shape of these CV curves shows no obvious change, implying the excellent rate capability of the hierarchical core-shell array nanostructure. Notably, the anodic and cathodic peaks slightly shift towards higher and lower potential with increasing scan rates, respectively, which could be attributed

to the internal resistance and polarization effect of the electrode. To explain the charge storage mechanism, the relationship between the anodic/cathodic peak current (I_p) and the square root of the corresponding scan rate ($v^{1/2}$) is shown in the inset of Fig. 5b. Notably, the anodic and cathodic current increase linearly with the $v^{1/2}$ at all scan rates, indicating that the redox reaction is a diffusion-controlled process.[53,56,57]

Fig. 5c shows the galvanostatic charge-discharge curves to further pledge the application potential of the as-synthesized hybrid structure as an electrode at different current densities (3, 5, 10, 15 and 20 A g^{-1}) in the potential window of 0-0.45 V (vs. Hg/HgO). The charge/discharge curves depict a quintessential deviation from a straight and flat line, which is consistent with the CV curves, demonstrating that the capacitance mainly stems from the Faradic pseudocapacitance. It could be clearly found that the galvanostatic discharge curves consist of two regions: 0.25-0.45 and 0-0.25 V (vs. Hg/HgO). In the former region, the potential varies quickly against time so the discharge duration is quite short as a consequence of pure electric double-layer capacitance from the charge separation on the electrode/electrolyte interface. On the other hand, in the latter region, the potential changes slowly against the time with much longer discharge duration, indicating that the capacitance predominately originates from pseudocapacitance due to electrochemical adsorption or rapid redox reaction on the interface between electrode and electrolyte. The specific capacitances are calculated to be 1471, 1196, 1111, 1040, 973 F g^{-1}, respectively, at various current densities. The specific capacitance of $ZnCo_2O_4$ and PCF@$ZnCo_2O_4$ electrodes can be calculated from the CV curves according to Eq. (1) and the calculated specific capacitance as a function of scan rates is plotted in Fig. 5d. The PCF@$ZnCo_2O_4$ hybrid electrode exhibits a high specific capacitance of 1384 F g^{-1} at 2 mV s^{-1}, which is much higher than that of $ZnCo_2O_4$ electrode (367 F g^{-1}) and PCF@Co_3O_4 electrode (267 F g^{-1}, Fig. S1a) at the same scan rate. Although the specific capacitance decreases gradually with the increase of scan rate, a high value of 841 F g^{-1} can still be maintained even at 50 mV s^{-1} for PCF@$ZnCo_2O_4$ hybrid electrode with a retention ratio of 61%, much higher than that of pure

$ZnCo_2O_4$ (39.3%) and PCF@Co_3O_4 (14.3%) (Fig. S1b) electrodes. This phenomenon may be explained as follows: Zn ions occupy the tetrahedral site in the cubic spinel structure and the trivalent Co ions occupy the octahedral sites. It is well-known that the zinc compounds have high electrical conductivity and could act as conductive highways for the charge accumulation and transfer of electrons.[49] During the electrochemical process, it can improve the electrical conductivity and offer rich redox chemistry, giving rise to further improvement of the overall performance of the electrode material.[34]

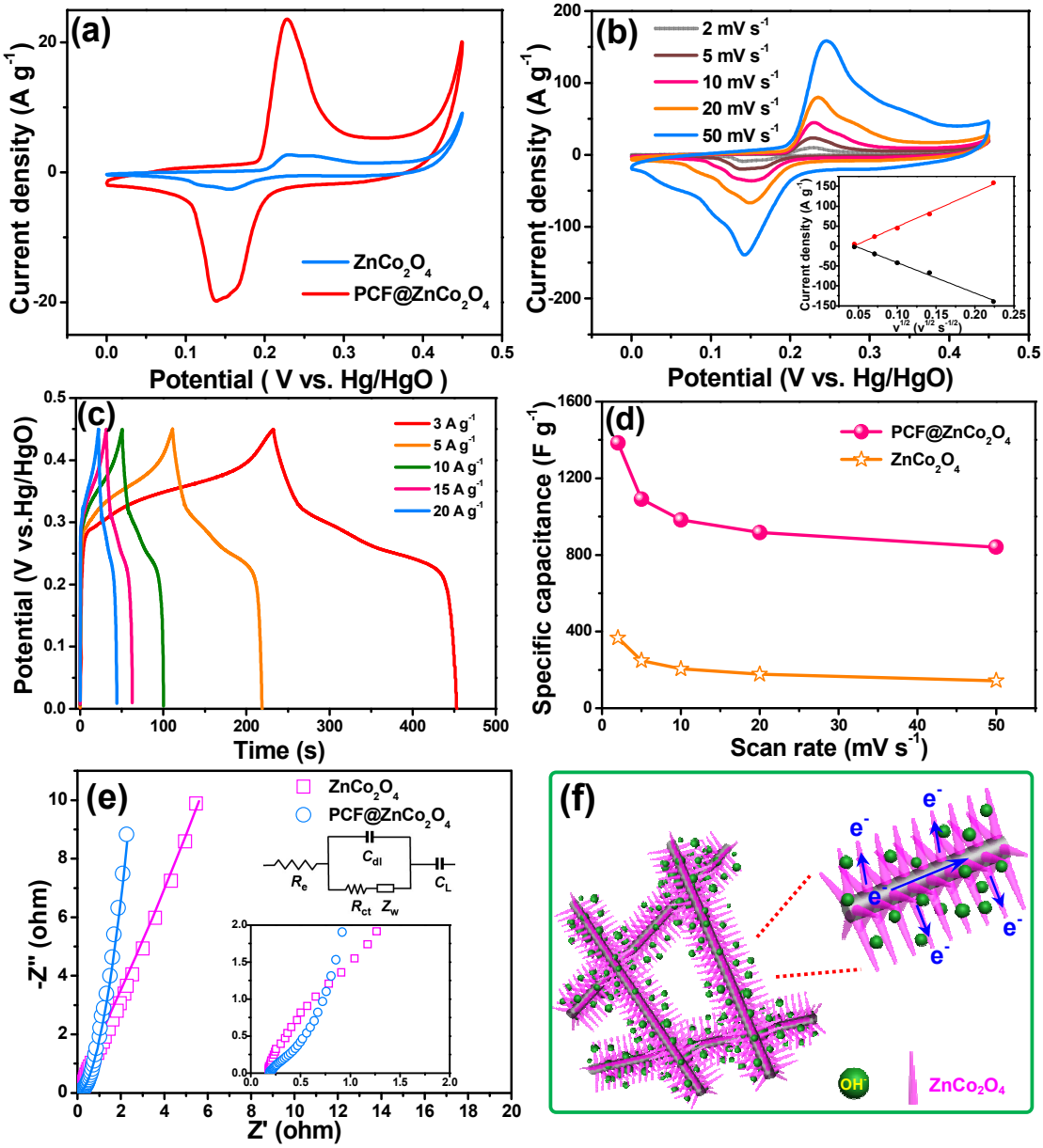

Fig. 5. (a) CV curves of $ZnCo_2O_4$ and PCF@$ZnCo_2O_4$ electrodes at the scan rate of 2 mV s^{-1}. (b) CV curves of PCF@$ZnCo_2O_4$ hybrid electrode at various scan rates ranging from 2 to 50 mV s^{-1} (Inset is the relationship between the peak currents and the square root of the corresponding scan rates in CV curves). (c) Galvanostatic charge-discharge curves of PCF@$ZnCo_2O_4$ electrode at different current densities. (d) Specific capacitance calculated from CV curves as a function of scan rates. (e) Nyquist plots of experimental impedance data (scattering dot) and fitting results (solid line) measured at the open circuit potential in the frequency range from 100 kHz to 0.01 Hz. Insets: the electrical equivalent circuit used for fitting impedance spectra and the high-frequency region. (f) Schematic illustration of the charge storage mechanism of the PCF@$ZnCo_2O_4$ hybrid.

Fig. 5e illustrated the electrochemical impedance spectroscopy (EIS) measurements performed of $ZnCo_2O_4$ and PCF@$ZnCo_2O_4$ hybrid electrode at a frequency range from 100 kHz to 0.01 Hz with a perturbation-potential amplitude of 5 mV. In the high frequency region, there is no distinct semi-circle in the high-to-medium frequency region for the Nyquist plot of PCF@$ZnCo_2O_4$ hybrid compared with $ZnCo_2O_4$ electrode, suggesting high ionic conductivity and fast electron transfer kinetics of the redox reaction at the electrode interface.[33,58] In the low frequency region, the slope of the curves shows the Warburg resistance, which represents the ion diffusion of electrolyte to the electrode surface. Compared with the $ZnCo_2O_4$ electrode, the PCF@$ZnCo_2O_4$ hybrid electrode presents a more vertical straight line along the imaginary axis, suggesting its much lower diffusion resistance. This can be attributed to the highly porous structure with large surface area which enables the enhanced electrolyte penetration and ion diffusion in the host materials. More detailed analysis was carried out using the complex nonlinear least-squares (CNLS) fitting method. The Nyquist plots were well-fit to the equivalent circuit as shown in the inset of Fig. 5e. Rs is the series solution resistance, which may include the electrolyte resistance and the active material/current collector contact resistance. C_{dl} represent double-layer capacitance, R_{ct} is the charge transfer resistance at the electrode/solution interface, Z_w is the ion diffusion controlled Warburg impedance, and C_L is the limit

pseudocapacitance.[40] Table 1 shows obtained values of R_s, C_{dl}, R_{ct}, Z_w and C_L calculated from CNLS fitting of the experimental impedance spectra. The R_s and R_{ct} of the $ZnCo_2O_4$ electrode are 0.227 and 0.547 Ω, while those of PCF@$ZnCo_2O_4$ electrode are 0.197 and 0.075 Ω, respectively, indicating a well-connected interface nature of electrolyte ions and electrode after the introduction of conductive PCF substrate.

The superior electrochemical performance of the PCF@$ZnCo_2O_4$ electrode could be attributed to the following aspects as shown in Fig. 5f. First, the PCFs serve as substrates, which provide a large surface area (1939 m^2 g^{-1}) for the growth of $ZnCo_2O_4$ nanoneedle arrays and accelerate electron transport for the Faradic reaction due to their intrinsically excellent electrical conductivity. Second, the porous structure in $ZnCo_2O_4$ nanoneedle arrays could effectively facilitate the electrolyte transport, enhancing the electrochemical kinetics and ensuring efficient interfacial contact between the active material and the electrolyte. Third, hierarchical PCF@$ZnCo_2O_4$ provides loose textures and open spaces between neighboring hybrid fibers, ensuring that the electrolyte ions readily penetrate into the inner region of the electrode, greatly shortening the transport/diffusion paths of electrolyte ions and increasing the utilization of the active materials. More importantly, the unique hierarchical core-shell structure could efficiently inhibits the volume changes during the charge-discharge process. Finally, the PCF@$ZnCo_2O_4$ hybrid are directly used as electrode without the use of carbon black and polymer binder, avoiding the use of "inactive" materials and improving the availability of active materials.[38]

Table 1. The calculated values of R_s, C_{dl}, R_{ct}, Z_w and C_L through CNLS fitting of the experimental impedance spectra based upon the proposed equivalent circuit in Fig. 5e.

	R_s (Ω)	C_{dl} (F)	R_{ct} (Ω)	Z_w	C_L (F)
$ZnCo_2O_4$	0.227	0.0348	0.547	0.0332	0.00267
PCF@$ZnCo_2O_4$	0.197	0.0945	0.0750	0.0262	0.00590

3.3. Electrochemical characterization of PCFs

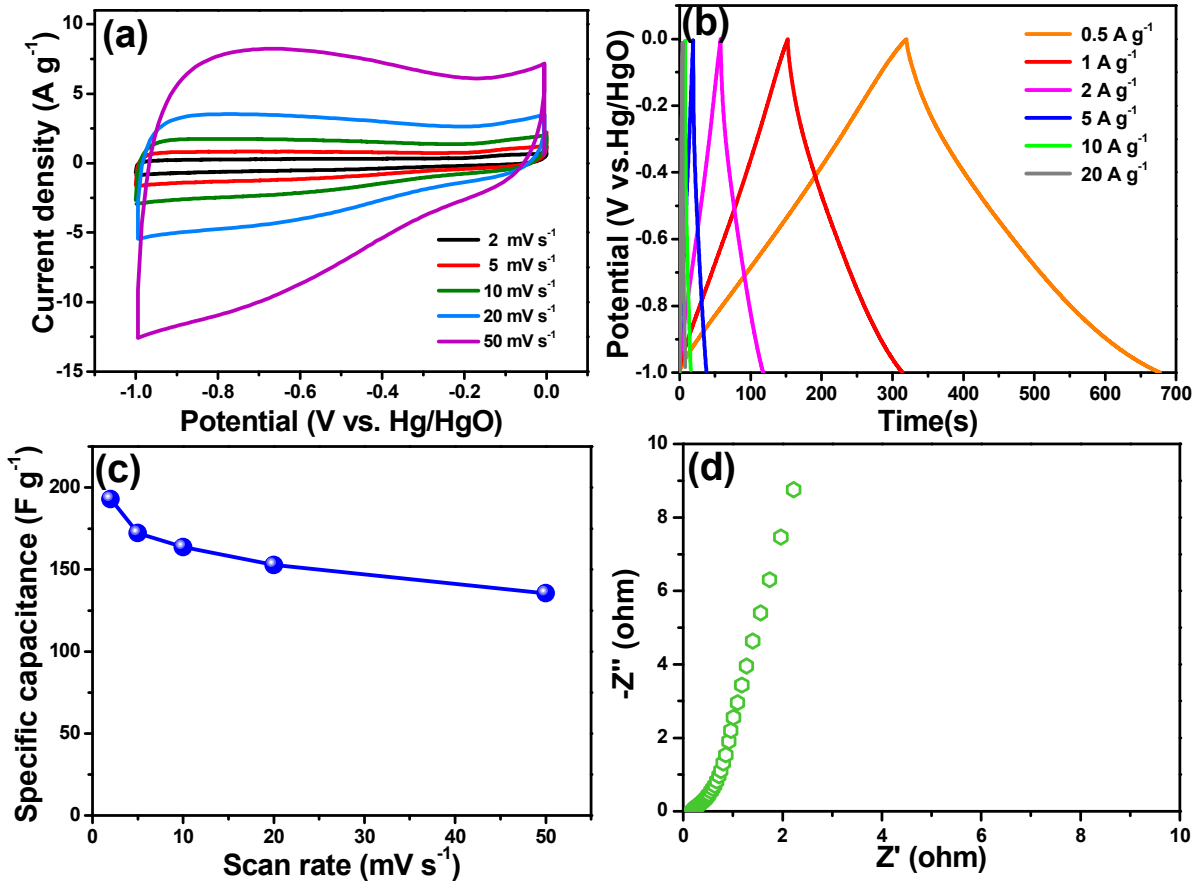

Fig. 6. (a) CV and (b) galvanostatic charge/discharge curves of the PCF electrode at different scan rates and current densities within a potential range of -1 to 0 V (vs. Hg/HgO) in 6 M KOH. (c) Specific capacitance of PCF electrode at various scan rates. (d) Nyquist plot of the PCF electrode in the frequency range of 100 kHz to 0.01 Hz.

Fig. 6a shows the CV curves of PCF electrode with the scan rates from 2 to 50 mV s^{-1} between -1 and 0 V (vs. Hg/HgO). Obviously, all the CV curves show nearly ideal rectangular shapes without visible distortion even at the scan rate of 50 mV s^{-1}, indicating that the PCF electrode has an ideal supercapacitor behavior. Typical galvanostatic charge/discharge curves of PCF electrode at different current densities from 0.5 to 20 A g^{-1} are displayed in Fig. 6b. It can be seen that all the charge and discharge curves are highly symmetric, suggesting that the electrode possesses an ideal capacitive performance and splendid electrochemical reversibility. Moreover, the specific capacitance of the

PCF electrode calculated according to the CV curves are presented in Fig. 6c. A specific capacitance of 193 F g^{-1} is achieved at the scan rate of 2 mV s^{-1} and remains 136 F g^{-1} when the scan rate increases to 50 mV s^{-1}. Fig. 6d displays the EIS analysis of the PCF electrode. As it can be seen, the equivalent series resistance is 0.19 Ω, indicating high charge and discharge rate of PCF electrode. Notably, no obvious semi-circle of the EIS plot can be observed, demonstrating fast charge transfer towards the surface of the electrode.

3.4. Electrochemical characterization of the all-solid-state ASC device

To further evaluate the capacitive performance of PCF@$ZnCo_2O_4$ towards real applications, all-solid-state ASC supercapacitor device was assembled using the as-prepared PCF@$ZnCo_2O_4$ hybrid and PCFs as the positive and negative electrode, respectively, with PVA/KOH electrolyte and cellulose filter paper as the separator. Fig. 7a presents the corresponding voltage windows of the PCF@$ZnCo_2O_4$ hybrid and PCF electrode at a scan rate of 5 mV s^{-1}, demonstrating that they can be assembled into an ASC device due to the different potential windows. Fig. 7b shows the CV curves of the fabricated ASC at different voltage windows recorded at a scan rate of 20 mV s^{-1}. As expected, the stable operating voltage can be extended up to 1.6 V. The CV curves of the fabricated ASC at different scan rates in a voltage window of 0-1.6 V are shown in Fig. 7c. The two broad redox peaks in each curve indicate the pseudocapacitive property of the supercapacitor due to Faradic redox reactions. According to the CV curves of the ASC device, the specific capacitance based on the total mass of materials in two electrodes is calculated to be 139.2 F g^{-1} at 2 mV s^{-1} and retains 67.3 F g^{-1} at 50 mV s^{-1} as shown in Fig. 7d. Energy and power densities are two vital parameters to characterize the electrochemical performance of supercapacitor devices. Fig. 7e shows the Ragone plot of the fabricated PCF@$ZnCo_2O_4$//PCF ASC device. The all-solid-state ASC could achieve a high energy density of 49.5 Wh kg^{-1} at a power density of 222.7 W kg^{-1}, which is highly comparable to the previously reported $ZnCo_2O_4$ based ASC devices, such as $ZnCo_2O_4$@MnO_2//α-Fe_2O_3 (37.8 Wh

kg^{-1}),[33] $ZnCo_2O_4$//activated carbon (41 Wh kg^{-1}),[30] $ZnCo_2O_4$//porous nanotubes (25 Wh kg^{-1}),[59] $ZnCo_2O_4$/PPy//PPy (30.9 Wh kg^{-1}).[60]

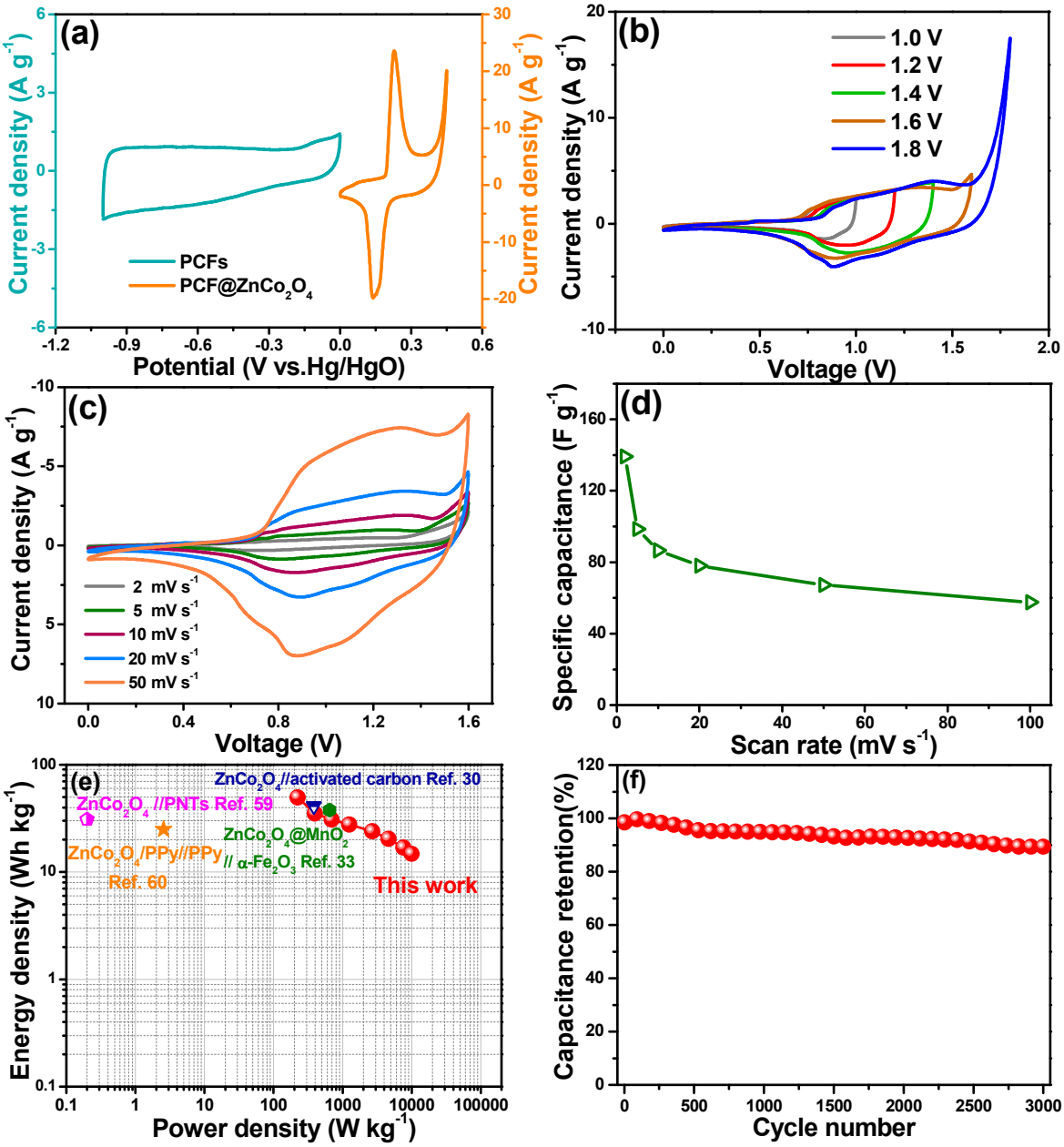

Fig. 7. (a) CV curves of PCFs and PCF@$ZnCo_2O_4$ electrodes performed in a three-electrode cell in 6 M KOH aqueous solution at a scan rate of 5 mV s^{-1}. (b) CV curves of the PCF@$ZnCo_2O_4$//PCFs all-solid-state ASC device measured at different voltage windows with PVA/KOH polymer electrolyte. (c) CV curves of the device at various scan rates. (d) Specific capacitance as a function

of scan rates. (e) Ragone plot of the PCF@$ZnCo_2O_4$//PCFs all-solid-state ASC device and the values reported previously ($ZnCo_2O_4$@MnO_2//α-Fe_2O_3,[33] $ZnCo_2O_4$//activated carbon,[30] $ZnCo_2O_4$//porous nanotubes,[59] $ZnCo_2O_4$/PPy//PPy.[60]). (f). Cycling performance of the all-solid-state ASC device measured at 50 mV s^{-1} over 3000 cycles.

Since the long-term cyclic stability of supercapacitors is another crucial requirement in practical application, the cycling stability of the ASC device was evaluated through repeating the CV test between 0 and 1.6 V at a scan rate of 50 mV s^{-1} for 3000 cycles (Fig. 7f). About 90% of its initial capacitance is retained after 3000 cycles, demonstrating superior cycling stability of our fabricated ASC device. The XRD pattern and SEM image of the PCF@$ZnCo_2O_4$ heterostructure after the cycling test are shown in Fig. S2. As shown in the XRD pattern (Fig. S2a), the diffraction peaks can be well indexed to cubic spinel $ZnCo_2O_4$ phase (JCPDS card no. 23-1390) except those peaks ascribed to metal Ni. Additionally, the hybrid still remains its inital core-shell naostrucures after cycling test (Fig. S2b), suggesting a stable structure of PCF@$ZnCo_2O_4$.

It is generally accepted that the total energy stored in a single cell can not satisfy the power and energy requirements for most practical applications. Thus, in order to form a reasonable specific voltage and capacitance rating for some practical microelectronic applications, supercapacitors need to be connected together in series or parallel combinations.[61,62] Fig. 8a exhibits the galvanostatic charge/discharge curves of a single device and the two devices connected in series. The operating voltage window of the series (3.2 V) is widened double that of a single device. Fig 8b shows the galvanostatic charge/discharge curves of the two connected in parallel. Compared to a single device, the overall capacitance is two times by a factor of two under the same voltage window of 0 to 1.6 V. The discharge time is about two times longer than that of a single device, which also attests the good capacitive performance in parallel assembly. To highlight its potential application, our fabricated all-solid-state ASC was used to light commercial red light-emitting diode (LED). Impressively, the two all-solid-state ASC devices connected in series are capable of simultaneously lighting up eight

red LEDs after being charged to 3.2 V (Fig. 8c), demonstrating the excellent practical application potentials of the devices for energy storage system.

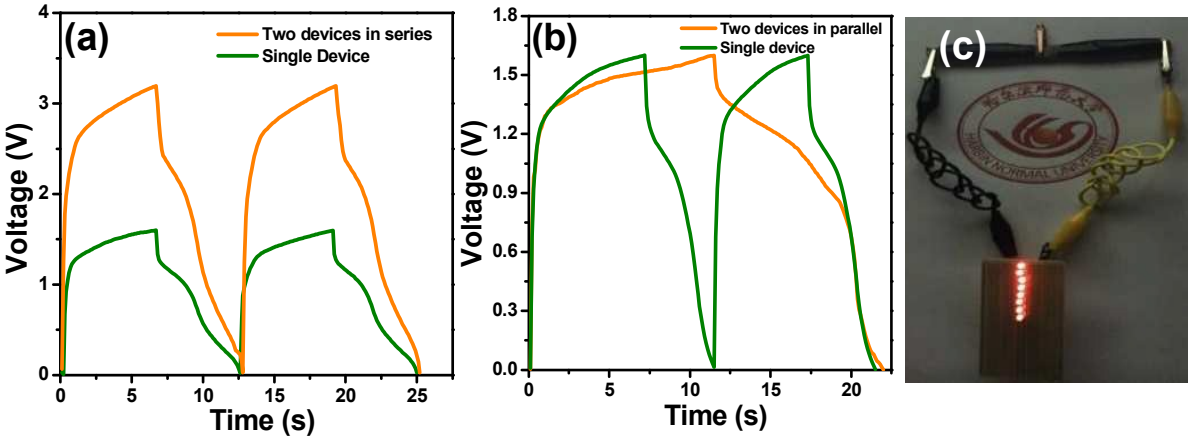

Fig. 8. Galvanostatic charge/discharge curves of a single all-solid-state supercapacitor and two supercapacitor in (a) series and (b) parallel. (c) Two assembled all-solid-state ASC devices connected in series to simultaneously light up eight red LEDs.

4. Conclusions

In summary, the hierarchical PCF@$ZnCo_2O_4$ nanoneedle has been successfully synthesized. The as-obtained PCF@$ZnCo_2O_4$ electrode exhibits a high specific capacitance of 1384 F g^{-1} at the scan rate of 2 mV s^{-1}. Additionally, an all-solid-state ASC device based on PCF@$ZnCo_2O_4$ and PCFs are well designed. The fabricated and optimized ASC device exhibits a high energy density of 49.5 Wh kg^{-1}, which is highly comparable to the previously reported $ZnCo_2O_4$ based ASC systems, and superior cycling stability (90% capacitance retention after 3000 cycles). Moreover, an application of our high-performance ASC device has been demonstrated by switching red LEDs, endowing our all-solid-state ASC new opportunities as energy storage devices for various portable electronic systems.

Acknowledgements

The authors acknowledge the financial support from the National Natural Science Foundation of

China (21471041, 21171045), Natural Science Foundation of Heilongjiang Province of China (ZD201214), Technology Development Pre-project of Harbin Normal University (12XYG-11).

References

1. J. Xiao, L. Wan, S. Yang, F. Xiao and S. Wang, *Nano Lett.*, 2014, **14**, 831-838.
2. G. Zhang and X. W. Lou, *Adv. Mater.*, 2013, **25**, 976-979.
3. Q. Yang, Z. Lu, X. Sun and J. Liu, *Sci. Rep.*, 2013, **3**, 3537.
4. Q. Zhang, M. Q. Zhao, D. M. Tang, F. Li, J. Q. Huang, B. Liu, W. C. Zhu, Y. H. Zhang and F. Wei, *Angew. Chem. Int. Ed.*, 2010, **49**, 3642-3645.
5. J. Qu, L. Shi, C. He, F. Gao, B. Li, Q. Zhou, H. Hu, G. Shao, X. Wang and J. Qiu, *Carbon*, 2014, **66**, 485-492.
6. T. Zhai, F. Wang, M. Yu, S. Xie, C. Liang, C. Li, F. Xiao, R. Tang, Q. Wu, X. Lu and Y. Tong, *Nanoscale*, 2013, **5**, 6790-6796.
7. J. Yan, Q. Wang, C. Lin, T. Wei and Z. Fan, *Adv. Energy Mater.*, 2014, **4**, 1400500.
8. S. Feng, W. Li, J. Wang, Y. Song, A. A. Elzatahry, Y. Xia and D. Zhao, *Nanoscale*, 2014, **6**, 14657-14661.
9. H. Niu, D. Zhou, X. Yang, X. Li, Q. Wang and F. Qu, *J. Mater. Chem. A*, 2015, **3**, 18413-18421.
10. C. Zhang, H. Yin, M. Han, Z. Dai, H. Pang, Y. Zheng, Y.-Q. Lan, J. Bao and J. Zhu, *ACS Nano*, 2014, **8**, 3761-3770.
11. X. Zhao, Q. Zhang, C.-M. Chen, B. Zhang, S. Reiche, A. Wang, T. Zhang, R. Schlögl and D.-S. Su, *Nano Energy*, 2012, **1**, 624-630.
12. S. Gao, Y. Sun, F. Lei, L. Liang, J. Liu, W. Bi, B. Pan and Y. Xie, *Angew. Chem. Int. Ed.*, 2014, **53**, 12789-12793.

13. C.-M. Chen, Q. Zhang, M.-G. Yang, C.-H. Huang, Y.-G. Yang and M.-Z. Wang, *Carbon*, 2012, **50**, 3572-3584.

14. Y.-Z. Liu, C.-M. Chen, Y.-F. Li, X.-M. Li, Q.-Q. Kong and M.-Z. Wang, *J. Mater. Chem. A*, 2014, **2**, 5730-5737.

15. W. Lv, D.-M. Tang, Y.-B. He, C.-H. You, Z.-Q. Shi, X.-C. Chen, C.-M. Chen, P.-X. Hou, C. Liu and Q.-H. Yang, *ACS Nano*, 2009, **3**, 3730-3736.

16. Y. Zhu, C. Cao, S. Tao, W. Chu, Z. Wu and Y. Li, *Sci. Rep.*, 2014, **4**, 5787.

17. Y. Z. Zhang, J. Zhao, J. Xia, L. Wang, W. Y. Lai, H. Pang and W. Huang, *Sci. Rep.*, 2015, **5**, 8536.

18. M. Huang, Y. Zhang, F. Li, Z. Wang, Alamusi, N. Hu, Z. Wen and Q. Liu, *Sci. Rep.*, 2014, **4**, 4518.

19. J. Zhao, J. Chen, S. Xu, M. Shao, Q. Zhang, F. Wei, J. Ma, M. Wei, D. G. Evans and X. Duan, *Adv. Funct. Mater.*, 2014, **24**, 2938-2946.

20. J. Yan, Q. Wang, T. Wei and Z. Fan, *Adv. Energy Mater.*, 2014, **4**, 1300816.

21. H. Wang, H. S. Casalongue, Y. Liang and H. Dai, *J. Am. Chem. Soc.*, 2010, **132**, 7472-7477.

22. P. Yang, Y. Ding, Z. Lin, Z. Chen, Y. Li, P. Qiang, M. Ebrahimi, W. Mai, C. P. Wong and Z. L. Wang, *Nano Lett.*, 2014, **14**, 731-736.

23. D. Zhou, H. Lin, F. Zhang, H. Niu, L. Cui, Q. Wang and F. Qu, *Electrochim. Acta*, 2015, **161**, 427-435.

24. X. Zhang, Y. Zhao and C. Xu, *Nanoscale*, 2014, **6**, 3638-3646.

25. S. Hou, G. Zhang, W. Zeng, J. Zhu, F. Gong, F. Li and H. Duan, *ACS Appl. Mater. Interfaces*, 2014, **6**, 13564-13570.

26. H.-P. Cong, X.-C. Ren, P. Wang and S.-H. Yu, *Energy Environ. Sci.*, 2013, **6**, 1185-1191.
27. F. Liu, G. Han, Y. Chang, D. Fu, Y. Li and M. Li, *J. Appl. Polym. Sci.*, 2014, **131**, 39779.
28. Y. Chen, M. Han, Y. Tang, J. Bao, S. Li, Y. Lan and Z. Dai, *Chem. Commun.*, 2015, **51**, 12377-12380.
29. H. Chen, L. Hu, M. Chen, Y. Yan and L. Wu, *Adv. Funct. Mater.*, 2014, **24**, 934-942.
30. B. Guan, D. Guo, L. Hu, G. Zhang, T. Fu, W. Ren, J. Li and Q. Li, *J. Mater. Chem. A*, 2014, **2**, 16116-16123.
31. H. Hu, B. Guan, B. Xia and X. W. Lou, *J. Am. Chem. Soc.*, 2015, **137**, 5590-5595.
32. Y. Xu, X. Wang, C. An, Y. Wang, L. Jiao and H. Yuan, *J. Mater. Chem. A*, 2014, **2**, 16480-16488.
33. W. Ma, H. Nan, Z. Gu, B. Geng and X. Zhang, *J. Mater. Chem. A*, 2015, **3**, 5442-5448.
34. K.-Y. Chun and I. K. Moon, *RSC Adv.*, 2015, **5**, 807-811.
35. B. Liu, B. Liu, Q. Wang, X. Wang, Q. Xiang, D. Chen and G. Shen, *ACS Appl. Mater. Interfaces*, 2013, **5**, 10011-10017.
36. B. Guan, D. Guo, L. Hu, G. Zhang, T. Fu, W. Ren, J. Li and Q. Li, *J. Mater. Chem. A*, 2014, **2**, 16116-16123.
37. S. Wang, J. Pu, Y. Tong, Y. Cheng, Y. Gao and Z. Wang, *J. Mater. Chem. A*, 2014, **2**, 5434-5440.
38. Q. Wang, L. Zhu, L. Sun, Y. Liu and L. Jiao, *J. Mater. Chem. A*, 2015, **3**, 982-985.
39. J. Cheng, Y. Lu, K. Qiu, H. Yan, X. Hou, J. Xu, L. Han, X. Liu, J.-K. Kim and Y. Luo, *Phys. Chem. Chem. Phys.*, 2015, **17**, 17016-17022.
40. K. Qiu, Y. Lu, D. Zhang, J. Cheng, H. Yan, J. Xu, X. Liu, J.-K. Kim and Y. Luo, *Nano Energy*, 2015, **11**, 687-696.

41. X. Lu, M. Yu, G. Wang, T. Zhai, S. Xie, Y. Ling, Y. Tong and Y. Li, *Adv. Mater.*, 2013, **25**, 267-272.

42. L. Bao, J. Zang and X. Li, *Nano Lett.*, 2011, **11**, 1215-1220.

43. Y. Dong, H. Lin, D. Zhou, H. Niu, Q. Jin and F. Qu, *Electrochim. Acta*, 2015, **159**, 116-123.

44. D. Zhou, Y. Dong, L. Cui, H. Lin and F. Qu, *J. Nanopart. Res.*, 2014, **16**, 1-9.

45. W. Li, F. Zhang, Y. Dou, Z. Wu, H. Liu, X. Qian, D. Gu, Y. Xia, B. Tu and D. Zhao, *Adv. Energy Mater.*, 2011, **1**, 382-386.

46. X. Yang, F. Qu, H. Niu, Q. Wang, J. Yan and Z. Fan, *Electrochim. Acta*, 2015, **180**, 287-294.

47. B. Liu, J. Zhang, X. Wang, G. Chen, D. Chen, C. Zhou and G. Shen, *Nano Lett.*, 2012, **12**, 3005-3011.

48. R. Madhu , V. Veeramani , S.-M. Chen, P. Veerakumar and S.-B. Liu, *Chem. Eur. J.*, 2015, **21**, 8200-8206.

49. F. Bao, X. Wang, X. Zhao, Y. Wang, Y. Ji, H. Zhang and X. Liu, *RSC Adv.*, 2014, **4**, 2393-2397.

50. C. Yuan, J. Li, L. Hou, X. Zhang, L. Shen and X. W. D. Lou, *Adv. Funct. Mater.*, 2012, **22**, 4592-4597.

51. W. Hu, R. Chen, W. Xie, L. Zou, N. Qin and D. Bao, *ACS Appl. Mater. Interfaces*, 2014, **6**, 19318-19326.

52. D. Kong, J. Luo, Y. Wang, W. Ren, T. Yu, Y. Luo, Y. Yang and C. Cheng, *Adv. Funct. Mater.*, 2014, **24**, 3815-3826.

53. Z. Wu, X. L. Huang, Z. L. Wang, J. J. Xu, H. G. Wang and X. B. Zhang, *Sci. Rep.*, 2014, **4**, 3669.

54. G. Zhang and X. W. David Lou, *Sci. Rep.*, 2013, **3**, 1470.

55. Q. Wang, J. Du, Y. Zhu, J. Yang, J. Chen, C. Wang, L. Li and L. Jiao, *J. Power Sources*, 2015, **284**, 138-145.

56. L. C. Wu, Y. J. Chen, M. L. Mao, Q. H. Li and M. Zhang, *ACS Appl. Mater. Interfaces*, 2014, **6**, 5168-5174.

57. J. Yan, W. Sun, T. Wei, Q. Zhang, Z. Fan and F. Wei, *J. Mater. Chem.*, 2012, **22**, 11494.

58. D. Cheng, Y. Yang, J. Xie, C. Fang, G. Zhang and J. Xiong, *J. Mater. Chem. A*, 2015, **3**, 14348-14357.

59. G. Zhou, J. Zhu, Y. Chen, L. Mei, X. Duan, G. Zhang, L. Chen, T. Wang and B. Lu, *Electrochim. Acta*, 2014, **123**, 450-455.

60. T. Chen, Y. Fan, G. Wang, Q. Yang and R. Yang, *RSC Adv.*, 2015, **5**, 74523-74530.

61. M. F. El-Kady and R. B. Kaner, *Nat. Commun.*, 2013, **4**, 1475.

62. H. Jin, L. Zhou, C. L. Mak, H. Huang, W. M. Tang and H. L. Wa Chan, *J. Mater. Chem. A*, 2015, **3**, 15633-15641.